PNAS Nexus, 2026, **5**, pgag366
https://doi.org/10.1093/pnasnexus/pgag366
Published: 24 October 2026
Research report

PNAS NEXUS OXFORD

Spatial organization of InSAR deformation-rate extremes across permafrost-transition and thermokarst contexts on the Tibetan Plateau

Mei Chen[1,2] **and Xie Hu**[1,2]*

[1]College of Urban and Environmental Sciences, State Key Laboratory of Vegetation Structure, Function and Construction (VegLab), and Key Laboratory for Earth Surface Processes of the Ministry of Education, Peking University, Beijing, China
[2]Beijing Key Laboratory of Spatio-temporal Perception and Urban Resilience, Peking University, Beijing, China
*To whom correspondence should be addressed: Email: hu.xie@pku.edu.cn
Guest Editor Xiyuan Bao
Accepted by Editor Barbara Romanowicz

Abstract

Ground motion in degrading permafrost (PF) terrain is uneven, and regional averages obscure the rare pixels—those with the most negative rates or the sharpest neighborhood contrasts—that matter most for infrastructure screening. Whether these extremes form organized, recurrent spatial groups or scattered anomalies has remained open. We analyzed the Sentinel-1 InSAR-estimated up-component rate during 2015–2021 and its spatial gradient along the Qinghai–Tibet Engineering Corridor, defining extremes separately within the mapped PF and nonpermafrost (NPF) domains. The extremes are spatially organized. Mapped transition segments contain 68.0% of NPF rate extremes and 71.3% of gradient extremes at 6.6 and 5.1 times interior prevalence, and PF rate extremes occur 2.4–6.5 times as frequently near mapped lakes, thaw slumps, or both as far from either inventory. Across 12 spatial evaluations, neighborhood differences in environmental variables consistently improved prediction of extremes at withheld pixels only within PF in the primary models. Among pixels retained after temporal quality control, roughly half of 2015–2021 extremes recurred in both 2015–2018 and 2019–2021, rising to 59–62% in the NPF transition, and within the same record, rate-selected pixels accumulated more negative line-of-sight displacement than matched nonextreme pixels in both viewing geometries. These map-referenced populations provide a transparent basis for screening and follow-up monitoring while supporting association-based interpretation rather than pixel-level attribution to thaw, thermokarst, or any single process.

Keywords permafrost degradation, deformation-rate extremes, thermokarst lakes and thaw slumps, InSAR, spatial machine learning

Significance Statement

The Qinghai–Tibet Engineering Corridor crosses warming permafrost (PF), where rare, strongly negative deformation signals matter more for infrastructure screening than regional averages. We show that InSAR-estimated deformation-rate extremes are spatially organized: 68–71% of nonpermafrost extremes cluster near the mapped PF boundary, while PF rate extremes cluster near lakes and thaw slumps. Neighborhood differences in environmental variables improve prediction of extremes at withheld pixels only within PF in the primary models, and recurrence among quality-retained pixels peaks at 59–62% near the mapped boundary. This organization provides a transparent, map-referenced basis for prioritizing screening and follow-up monitoring while separating observed deformation from unverified process attribution.

Introduction

Permafrost (PF) warming can lower ground surfaces and destabilize terrain (1, 2), weaken load-bearing conditions for roads and railways (3, 4), and alter drainage and ecosystems (5). The Qinghai–Tibet Engineering Corridor (QTEC) crosses warm, degrading plateau PF (6) in a deformation setting shaped by construction and other disturbance (7, 8), documented active-layer

Received: May 11, 2026. **Accepted:** October 12, 2026
© The Author(s) 2026. Published by Oxford University Press on behalf of National Academy of Sciences.
This is an Open Access article distributed under the terms of the Creative Commons Attribution-NonCommercial License (https://creativecommons.org/licenses/by-nc/4.0/), which permits non-commercial re-use, distribution, and reproduction in any medium, provided the original work is properly cited. For commercial re-use, please contact reprints@oup.com for reprints and translation rights for reprints. All other permissions can be obtained through our RightsLink service via the Permissions link on the article page on our site—for further information please contact journals.permissions@oup.com.

Downloaded from academic.oup.com/pnasnexus/article/5/11/pgag366/8997935 by Health Science Library of Peking University user on 10 November 2026

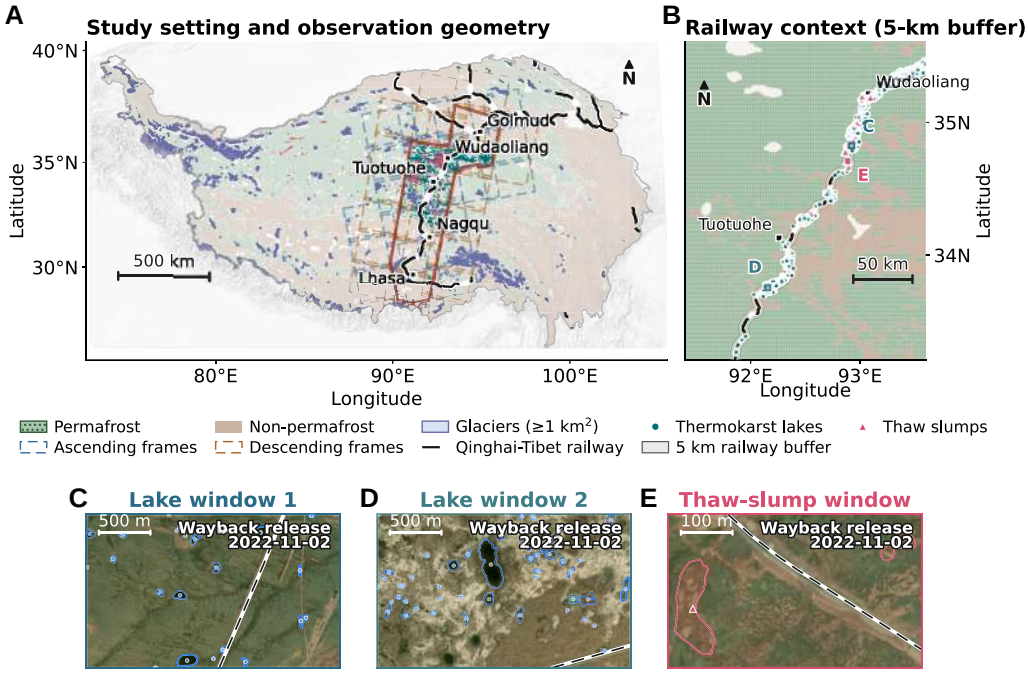


Figure 1 Study setting and observation geometry. PF/NPF, permafrost/nonpermafrost; QTEC, Qinghai–Tibet Engineering Corridor; DEM, digital elevation model. A) Plateau context with mapped PF/NPF, glaciers of at least 1 km^2, lake and slump inventories, Sentinel-1 frames, the railway, and corridor pixels; relief is an author-generated Copernicus DEM GLO-30 hillshade. B) The 5-km railway buffer and locator boxes for C–E. C–E) Georeferenced static-map windows from Esri World Imagery (Wayback release 2022–11–02); the underlying Maxar imagery was acquired 2020–06–24 (C, E) and 2020–10–10 (D), giving spatial context rather than time-matched validation. The three imagery panels use only whole-image display adjustments. Sources for C–E: Esri, Vantor/Maxar, Earthstar Geographics, and the GIS User Community; high-resolution imagery © Maxar. Map image is the intellectual property of Esri and is used herein under license. Copyright © 2026 Esri and its licensors. All rights reserved. The imagery is excluded from the data archive and from the article and archive Creative Commons licenses.

warming (9), engineered embankments (10), and abundant thermokarst lakes and thaw slumps (11, 12) (Fig. 1). Few transport corridors combine this density of lifeline infrastructure with mapped PF transitions and inventoried thermokarst landforms, making QTEC a diagnostic setting for linking regional deformation to mapped terrain context. Regional means describe broad motion but can obscure rare pixels where the estimated up-component rate is most negative or changes abruptly between neighboring pixels—signals potentially relevant to localized terrain instability and infrastructure screening. Corridor InSAR studies establish the value of regional monitoring (13), and related work addresses seasonal deformation and active-layer behavior over a broader interval (14), but PF InSAR remains sensitive to viewing geometry, environmental heterogeneity, temporal sampling, and reference choice (15, 16, 17). What remains open is whether the extreme tails form map-referenced spatial populations that persist across mapping and support choices, or scattered anomalies interpretable only case by case.

We use two complementary observations. The InSAR-estimated up-component rate, d_u, represents multiyear upward or downward motion under the zero-north-motion approximation used in the two-component east/up decomposition; negative values denote downward motion. Its spatial-gradient magnitude, $|\nabla d_u|$, measures how rapidly that rate changes between neighboring pixels in mm year^{-1} km^{-1}. The gradient is a spatial unevenness diagnostic, not a temporal derivative or mechanical strain. Both signals may reflect thaw-related settlement, slope-parallel or lateral motion, infrastructure-related movement (18), and residual atmospheric, processing, or geometric effects. An extreme value therefore identifies an unusual observation, not a process by itself. The two measures are termed targets below (Methods, InSAR deformation products and spatial context section).

Spatial context helps distinguish how the same rate should be interpreted near a mapped PF–NPF transition, beside a thermokarst landform, or in remaining PF-interior terrain. A corridor-wide cutoff would largely recover the broad PF–NPF contrast, so we define extremes relative to each mapped domain, meaning the PF or NPF area. The Zou product provides the primary stratification and distance datum (19), and the Cao product, representing conditions around 2010, provides an alternative historical boundary reference for sensitivity testing (20). Mapped lakes and slumps are contextual inventories, not complete activity records: regional observations document active slumps and rapid lake change (21, 22), diverse landform characteristics and trajectories (23, 24), and unavoidable inventory and susceptibility uncertainty (25, 26, 27). The regional design prioritizes spatial replication over detailed site histories: it can assess first-order organization across the corridor, whereas the 5-km railway buffer provides infrastructure context rather than defining the set of analyzed pixels.

Our design proceeds from observation through spatial partition and held-out model response to temporal recurrence. Boundary and inventory distances, withheld from every model, sort the extremes into mutually exclusive map-referenced groups (the spatial partition), each a population of pixels sharing the same geographic context. Models then test whether environmental variables at each pixel (raw variables) or their neighborhood differences (local contrasts) improve prediction at pixels withheld for evaluation, and total-domain and group-stratified accumulated local effects (ALE) summaries describe how those model responses differ among the populations, not causal effects (28).

Downloaded from academic.oup.com/pnasnexus/article/5/11/pgag366/8997935 by Health Science Library of Peking University user on 10 November 2026

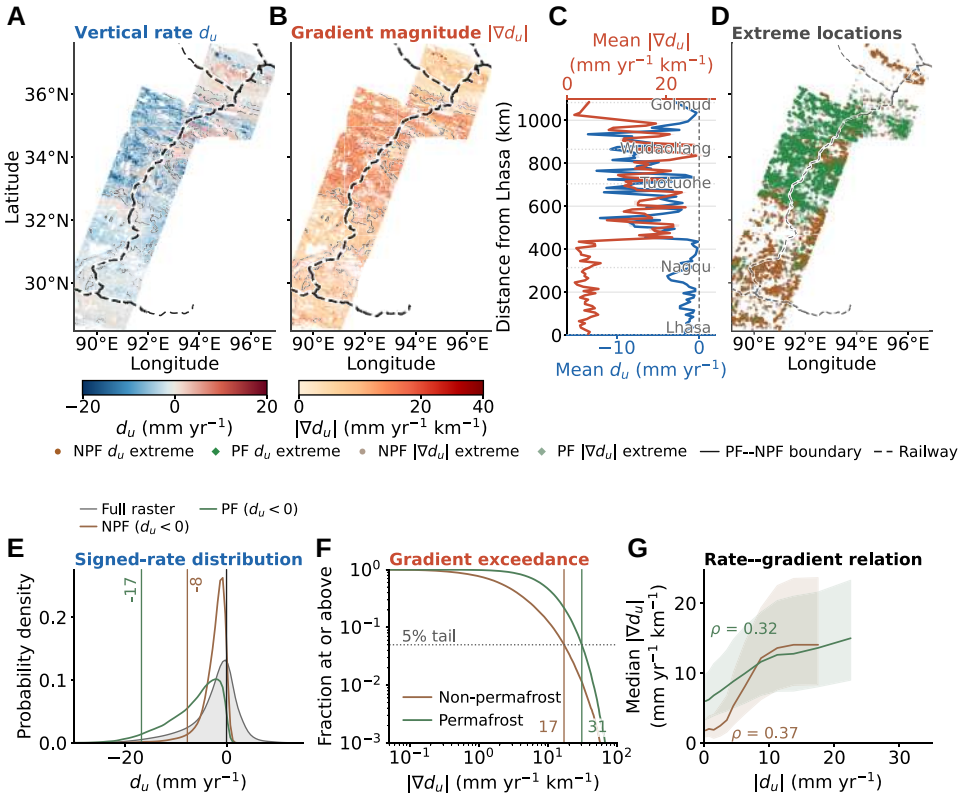


Figure 2 InSAR-estimated deformation and tail definitions. PF/NPF, permafrost/nonpermafrost; InSAR, interferometric synthetic aperture radar; d_u, estimated up-component rate; $|\nabla d_u|$, spatial-gradient magnitude. A, B) Signed approximately 2015–2021 up-component deformation rate and spatial-gradient magnitude, each with the mapped PF–NPF boundary and the railway. Color scales saturate at −20 and +20 mm year^{-1} for d_u and at 0 and 40 mm year^{-1} km^{-1} for the gradient. For page-scale legibility, the maps render every third native cell with a display-only gamma transformation ($\gamma = 0.60$) applied to the gradient and an ~2.5-km generalized contact line; analyses use native values and original classes. C) Mean profiles within the 1-km railway buffer plotted against distance from Lhasa; d_u and $|\nabla d_u|$ use independent scales, with corridor waypoints marked. D) Domain-specific tail-sample pixels: saturated markers show NPF and PF lower tail d_u extremes, and muted markers show upper-tail gradient extremes, with the railway for georeference. E) Full signed raster and domain-balanced negative-d_u distributions with thresholds. F) Domain gradient exceedance and thresholds. G) Median and interquartile gradient magnitude in fixed $|d_u|$ bins with per-domain Spearman ρ. Extreme samples and domain curves use the domain-balanced analysis sample. Gradient curves use 82,400 PF and 83,944 NPF pixels with finite native-grid gradients.

Finally, nonoverlapping time windows (2015–2018 and 2019–2021) assess which populations contain recurrent rather than window-specific extremes. Spatial blocking keeps contiguous geographic blocks of pixels together during model fitting or evaluation and reduces overstatement of independence in spatially correlated data (29, 30, 31). We ask four linked questions: how the PF and NPF tails differ; how boundary, lake, and slump distances organize them; whether local contrasts add skill beyond raw variables and how responses vary among the resulting geographic contexts; and which populations recur across time windows. Answering them turns scattered extreme values into map-referenced populations whose organization and recurrence can be tested across mapping and support choices, rather than asserted case by case.

Results

InSAR-estimated deformation differs between mapped domains

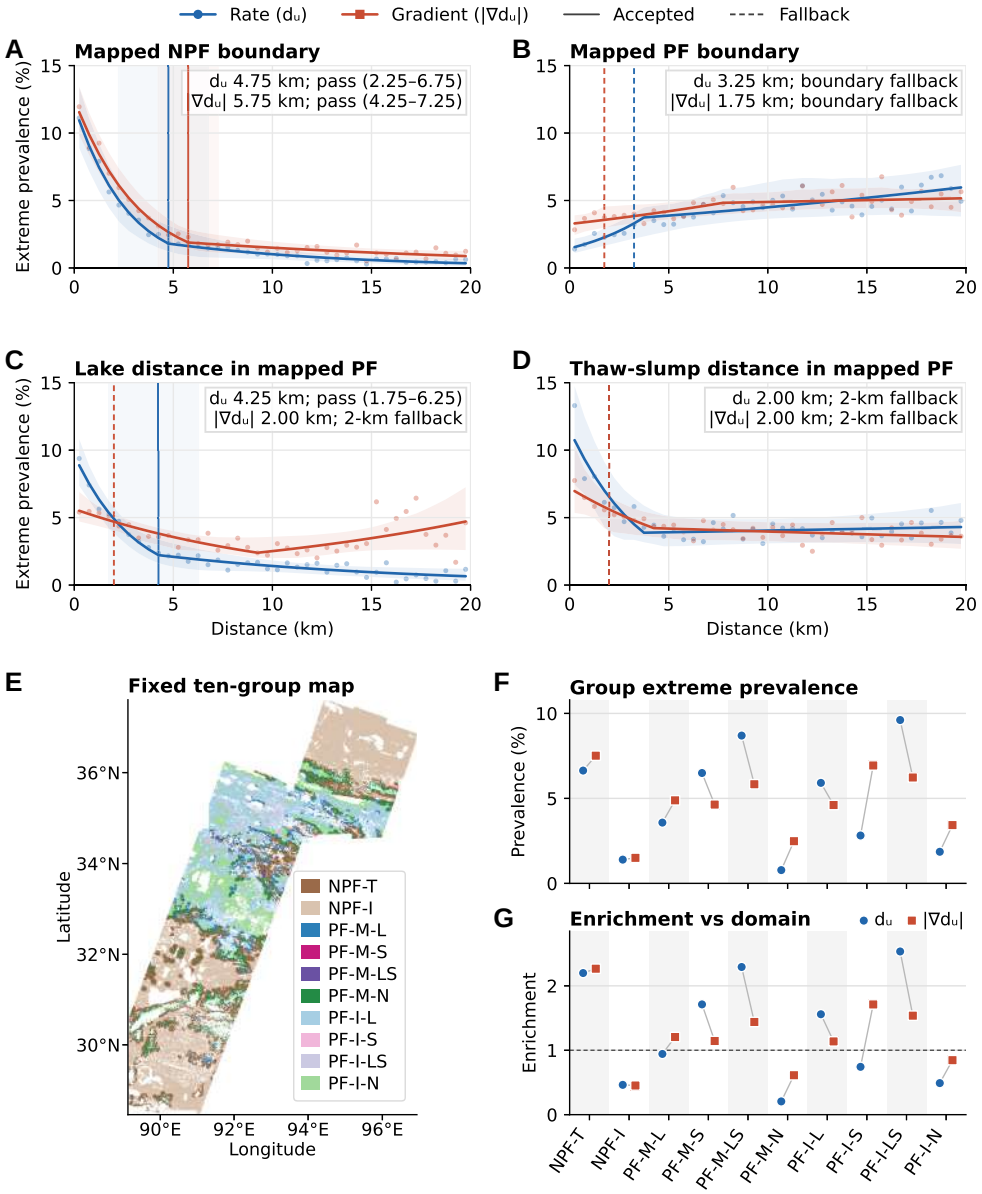
The full signed up-component field (rate map) during 2015–2021 contains both downward and upward motion; 68.5% of valid raster pixels are negative (Fig. 2A, E; Methods, Domain separation and extreme definitions section). We restricted the domain-balanced analysis sample to pixels with negative d_u so that both targets are evaluated within the negative- d_u subset. Within this sample, mapped PF has a more negative median d_u than mapped NPF (~−5 vs. −2 mm year^{-1}) and a larger median gradient magnitude (~9 vs. 3 mm year^{-1} km^{-1}; Fig. 2).

Domain-specific 5% tails give lower tail d_u thresholds near −17 mm year^{-1} in PF and −8 mm year^{-1} in NPF, and upper-tail gradient thresholds near 31 and 17 mm year^{-1} km^{-1}. We use these as analysis labels, not universal hazard thresholds; whether a pixel belongs to a tail is determined using unrounded values. Downward motion and gradient magnitude are positively but imperfectly related (Spearman $\rho = 0.32$ in PF, 0.37 in NPF), supporting complementary rather than interchangeable treatment (Fig. 2G).

Distance profiles define a complete map-referenced partition of eligible pixels

To test whether extremes concentrate near the mapped boundary, we fitted binomial hinge profiles on an ~0.95-km systematic sample of the valid deformation footprint, applying the primary

Downloaded from academic.oup.com/pnasnexus/article/5/11/pgag366/8997935 by Health Science Library of Peking University user on 10 November 2026



Operational distances summarize spatial profiles; groups are mapped contexts, not causal process classes.

Figure 3 Distance profiles and the fixed 10-group spatial partition. PF/NPF, permafrost/nonpermafrost; T/I, NPF transition/interior; M/I, PF margin/interior; L, S, LS, and N, lake-only, slump-only, both, and neither; d_u, up-component rate; A–D) Extreme-prevalence profiles for rate and gradient extremes on the systematic grid for the NPF boundary, PF boundary, and lake and thaw-slump distances in mapped PF; solid vertical lines show breakpoints meeting the prespecified criteria, and dashed vertical lines show operational fallbacks. E) Complete fixed d_u-derived partition of eligible pixels into two NPF boundary strata and eight PF margin/interior × lake/slump contexts. F) Prevalence of rate and gradient extremes within the geographic groups in (E). G) Each prevalence divided by the prevalence across all sampled PF or NPF pixels with valid data for that measure. In (F) and (G), circles and squares indicate rate and gradient extremes, respectively. Both panels use the distance boundaries selected for d_u; Table S12 reports groups defined separately for rate and gradient extremes. Lake-water pixels and uncovered pixels are not eligible for assignment; thresholds and group labels are operational map summaries, not physical influence radii or process classes.

model-sample domain-tail thresholds rather than recalculating quantiles on the systematic sample (Fig. 3; Methods, Distance profiles and the 10-group partition section). Prevalence is the fraction of sampled pixels classified as extreme. The NPF breakpoints met every prespecified support criterion at 4.75 km for d_u and 5.75 km for the gradient. These transition segments (the near-boundary NPF groups) contain 68.0 and 71.3% of the corresponding NPF extremes; their extreme prevalence is 6.56 and 5.06 times that farther into NPF within the 0–20-km profiles. The PF-side breakpoints did not meet the uncertainty criterion, so the partition uses explicitly labeled 3.25- and 1.75-km operational margin widths; PF pixels beyond them form the interior groups. Under those widths, PF d_u extremes are less prevalent in the margin than the interior (2.08% vs. 4.47%), and the gradient contrast is smaller (3.46% vs. 4.19%).

Within PF, under the geographic groups defined separately for rates and gradients, the d_u lake profile met the prespecified support criteria at 4.25 km, whereas the slump profile and both gradient-inventory profiles use the predefined 2-km fallback because their breakpoint intervals are too wide. The primary

Downloaded from academic.oup.com/pnasnexus/article/5/11/pgag366/8997935 by Health Science Library of Peking University user on 10 November 2026

inventory distance is measured to polygon area: deformation-valid pixels inside mapped lake water are excluded, while slump interiors remain at distance zero. For each target, the hierarchy assigns every eligible covered pixel to 1 of 10 groups. For d_u, extreme prevalence is 1.47% away from both inventories, 5.36% in lake-only context, 3.47% in slump-only context, and 9.55% in dual context. Thus lake-only, slump-only, and dual-context prevalences are 3.6, 2.4, and 6.5 times the inventory-distal value. The corresponding gradient ratios are 1.6, 1.8, and 1.9. Figure 3E–G instead uses the same rate-derived geographic groups for both measures, whereas Table S12 reports the target-specific values quoted here. Because thermokarst landforms are themselves abundant here, we also use a common 2-km radius to test these contrasts against the expectation set by that abundance. Relative to all systematically sampled PF pixels, rate-extreme prevalence within 2 km is enriched 1.86-fold near lakes (95% interval 1.65–2.12) and 2.22-fold near slumps (1.65–2.99), with weaker gradient enrichments of 1.31 and 1.55 (Fig. S10). A 1,999-replicate bootstrap of complete 50-km blocks does not resolve a lake × slump interaction for either target, so the dual group is not evidence of synergy.

Target-specific and fixed d_u partitions, true polygon-edge sensitivity, 1-, 2-, 5-, and 10-km operational radii, object counts, and sparse groups are reported in Fig. S10 and Tables S10 and S12. Sparse groups are retained and identified rather than merged. The maps therefore describe spatial contexts rather than process classes. Site imagery illustrates transition, lake- and slump-proximal, and remaining PF-interior settings without assigning a cause (Fig. S5; Table S5).

Gas-field anchors for Tainan, Sebei No. 1, and Sebei No. 2, digitized independently of the deformation data (±2 km), overlap northern NPF zones of strongly negative estimated up-component rate. This overlap is consistent with documented extraction-related deformation (32) but is insufficient to attribute the complete signal. Excluding 5-km buffers leaves the NPF threshold near −8 mm year^{-1} and rate-extreme recurrence at 55.4% rather than 57.1%; the fixed 3.25-km model-sample Zou transition/interior prevalence ratio increases from 5.359 to 6.155, and temperature variables remain top-ranked in all 12 spatial evaluation schemes (combinations of block size, grid origin, and random seed) (Fig. S15; Table S14).

Local contrasts add skill in PF, and model responses vary among groups

To test whether neighborhood differences help identify extremes, we compared raw variables, local contrasts, and both combined (Fig. 4; Methods, Raw-state and local-contrast models section). In mapped NPF, adding contrasts to raw variables produces mixed held-out changes: the median difference across the 12 schemes in average precision (AP, a score summarizing detection of extremes) is −0.0003 for d_u (positive in 5/12 schemes) and +0.0022 for the gradient (8/12), below the prespecified incremental-skill criterion. In mapped PF, the combined stack improves AP in all 12 schemes, with median gains of 0.0142 for d_u and 0.0119 for the gradient. Group-stratified models therefore use raw variables in NPF and the combined stack in PF. Separate component permutation indicates that permuting some contrast components reduces held-out AP, but correlated components can exchange importance and do not override the ablation result.

The prespecified ALE diagnostics summarize how predicted extreme probability varies with each environmental variable across geographic groups (Fig. 4; Methods, Group-stratified ALE section). Predicted extreme probability decreases as mean annual ground temperature (MAGT) increases in every supported NPF model. For d_u, the normalized effect strength is 0.221 in the transition and 0.123 in the NPF interior, while the ALE difference between the 90th and 10th percentiles of ground temperature is −0.091 and −0.009 on the raw prediction scale. Within PF, responses to the topographic wetness index (TWI) and normalized difference vegetation index (NDVI) meet the stability criteria for every supported d_u population, but the TWI response changes direction by spatial context: predicted probability decreases with TWI in lake-only groups and increases in several inventory-distal or dual-context groups. Predicted probability increases with NDVI across the supported d_u groups, and the NDVI response is directionally stable for all supported gradient populations, whereas the gradient response to TWI is unresolved for total PF and PF-interior dual context. Slump-only and PF-margin dual-context populations remain in the summaries but have insufficient support for independent ALE inference.

Recurrence differs among the fixed spatial populations

To test whether extreme motion recurs at the same pixels, temporal reconstruction used 12,107 acquisition records from 72 image frames; 112 of 196 evaluated pairs met the predefined quality criteria (Methods, Within-record temporal recurrence section). Reconstructed full-window d_u agrees with the published deformation field (Spearman $\rho \approx 0.95$; centered mean absolute error (MAE) near 1 mm year^{-1}), and the rederived gradient agrees at $\rho \approx 0.85$ with centered MAE near 3 mm year^{-1} km^{-1} (Fig. S11; Table S13). Among pixels retained after the primary temporal quality screening, 49.8% of full-window d_u extremes and 48.1% of gradient extremes recur in both 2015–2018 and 2019–2021 (95% intervals from 500 bootstrap replicates of 50-km blocks, 45.1–54.3% and 46.2–50.3%, respectively). Recurrence is lower in mapped PF (34.2 and 40.9%) than in mapped NPF (57.1 and 56.8%).

Applying the full-window rate-derived groups unchanged across time windows shows that recurrence in the NPF transition is 58.7% for d_u extremes and 61.5% for gradient extremes, compared with 55.1 and 51.1% in the NPF interior. Transition recurrence has a higher point estimate than interior recurrence for both targets under all five quality-screening schemes. Among supported PF groups, recurrence spans 31.5–41.9% for d_u and 38.3–47.3% for the gradient; intervals overlap, and the PF-margin slump-only and dual-context groups do not meet the requirement of eight extreme-containing blocks. Window-specific composition also differs: 51.4% of PF-interior dual-context d_u extremes are late-only, whereas 44.3% of inventory-distal PF-interior extremes are early-only (Fig. 5).

Recurrence estimates are sensitive to the choice of pixels retained after quality screening: the largest difference between the primary and unmasked supports is 0.065, above the prespecified 0.05 criterion, and overall recurrence crosses 50% across the five quality-screening schemes. Nevertheless, the NPF-over-PF direction holds in all 10 target–scheme comparisons. The temporal

Downloaded from academic.oup.com/pnasnexus/article/5/11/pgag366/8997935 by Health Science Library of Peking University user on 10 November 2026

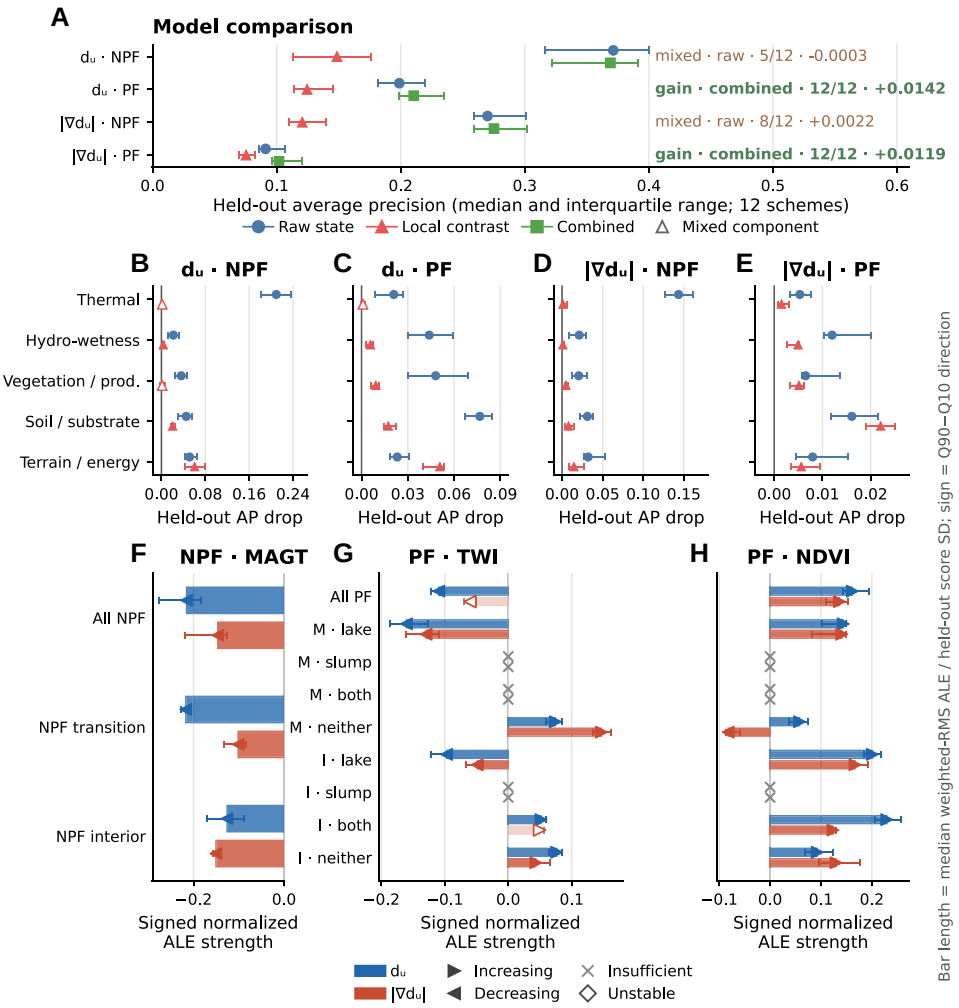


Figure 4 Raw environmental variables, local contrasts, and group-stratified model responses. PF/NPF, permafrost/nonpermafrost; T/I, NPF transition/interior; M/I, PF margin/interior; L/S/LS/N, lake-only/slump-only/both/neither; ALE, accumulated local effects; RMS, root mean square; SD, standard deviation; Thermal, temperature; Hydro-wetness, precipitation and wetness; Vegetation/prod., vegetation and productivity; Soil/substrate, soil properties; Terrain/energy, terrain and radiation; Raw state, raw variables. d_u, up-component rate; $|\nabla d_u|$, spatial-gradient magnitude. A) Held-out average precision (AP) for raw-only, contrast-only, and combined models; symbols and whiskers show medians and interquartile ranges across 12 spatial-blocking schemes, and right-hand labels give the prespecified incremental-contrast decision. B–E) Held-out AP loss after separately permuting raw-state and local-contrast members of each group of environmental variables; open symbols mark mixed or negligible stability. F–H) Signed, score-normalized ALE strength for the prespecified MAGT, TWI, and NDVI responses in total domains and supported groups. Bar length is median root mean square ALE (weighted by the fraction of evaluated pixels in each input bin) divided by the SD of their model scores; sign is ALE(Q_{90})—ALE(Q_{10}), where Q_{90} and Q_{10} are the 90th and 10th input percentiles; whiskers show interquartile ranges; crosses mark insufficient support; and open symbols mark unstable direction. All panels describe held-out spatial-classification behavior rather than causal effects.

crosswalk retains only 19–30% of original extreme pixels after primary quality control, so inference is conditional on retained support.

Paired displacement histories (displacement through time) compare extreme pixels with matched nonextreme controls from the same geographic group, 50-km block, and radar-frame pair (SI Methods S7b). Across the six supported mutually exclusive groups and four supported overlapping aggregate populations, d_u -selected pixels developed increasingly negative line-of-sight displacement relative to matched same-group controls in both viewing geometries. Trends in modeled displacement on 25 May each year (annual anchors) range from −10.7 to −5.7 mm year^{-1} in ascending data and from −9.0 to −4.3 mm yr^{-1} in descending data. All 120 population-by-geometry annual increments are negative with intervals excluding zero, and the largest step occurs between 2018 and 2019 in 19 of 20 population histories (one per population–geometry combination). Gradient-selected pixels, by contrast, show no systematic cross-geometry evolution in central-pixel line-of-sight displacement minus the median of its eight immediate neighbors (Fig. 5). Because selection and evaluation share the 2015–2021 record, the paired histories are descriptive population contrasts, not independent temporal validation.

Discussion

Boundary and inventory distances stratify distinct spatial populations

The supported NPF profiles, comparison with the alternative Cao map, and coordinate-shift sensitivity indicate a broad transition association that is not tied to one exact interface. They do not

Downloaded from academic.oup.com/pnasnexus/article/5/11/pgag366/8997935 by Health Science Library of Peking University user on 10 November 2026

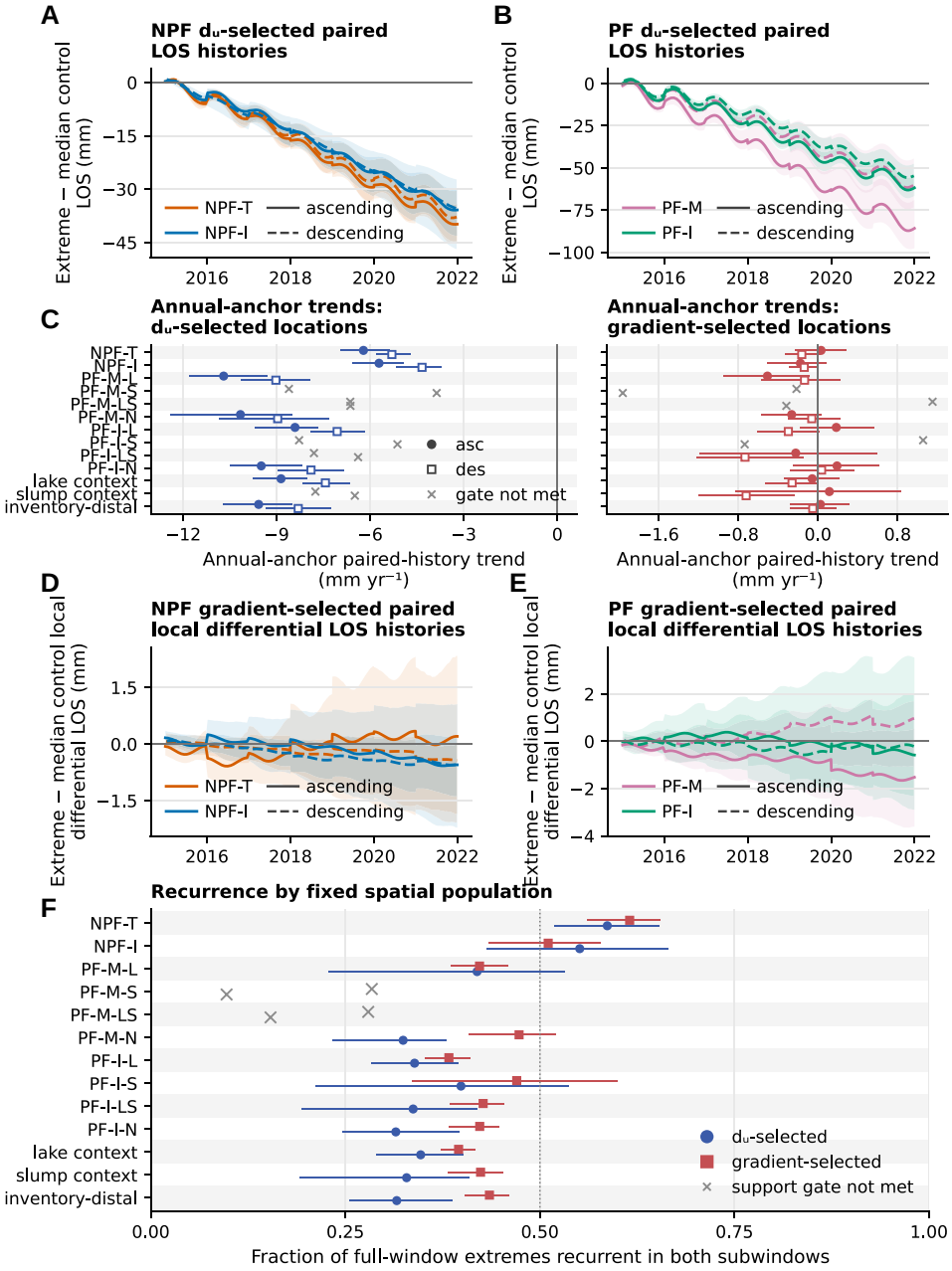


Figure 5 Temporal recurrence and paired deformation histories. The two targets are up-component rate, d_u, and its spatial-gradient magnitude, $|\nabla d_u|$. LOS, line of sight; asc/des, ascending/descending; PF/NPF, permafrost/nonpermafrost; T/I and M/I, transition/interior and margin/interior; L/S/LS/N, lake-only/slump-only/both/neither; and "any" combines inventory contexts. Controls are matched nonextreme pixels. A, B) Extreme-minus-control line-of-sight histories at d_u-selected pixels for the NPF transition and interior (NPF-T/NPF-I) and aggregate PF margin and interior (PF-M-any/PF-I-any). Solid and dashed lines indicate ascending and descending geometries; shading gives 95% intervals from 1,999 complete 50-km-block bootstrap replicates. C) Trends in modeled displacement on 25 May each year for both targets on separate scales across 10 mutually exclusive groups and selected PF aggregates; gray crosses mark insufficient support. D, E) Paired local differential line-of-sight histories at gradient-selected pixels. F) Fraction recurrent in both subwindows for 10 mutually exclusive groups and three PF aggregates; whiskers give 95% intervals where supported. Histories are descriptive contrasts conditional on retained support, not independent validation; the complete 10-group histories are shown in Fig. S12.

locate a contemporary thaw front: the maps predate the deformation interval and have kilometer-scale support, and the observed association may combine marginal PF, map disagreement, topography, hydrology, engineering disturbance, and viewing geometry. The fitted distances are therefore operational map summaries.

PF behavior differs, and this contrast is itself a result: boundary distance stratifies the NPF tail, whereas inventory context stratifies the PF tail. The PF-side breakpoint is imprecise, and the operational margin has lower rather than higher d_u-extreme prevalence. Most PF rate extremes instead occupy lake or dual-inventory contexts, while an inventory-distal population remains. Because thermokarst landforms are abundant across this terrain, proximity alone would be expected; enrichment relative to all systematically sampled PF pixels indicates that the association is not solely a consequence of landform density.

This spatial pattern is compatible with lake thermal and talik effects (33, 34, 35), ground-ice and hydrological pathways

Downloaded from academic.oup.com/pnasnexus/article/5/11/pgag366/8997935 by Health Science Library of Peking University user on 10 November 2026

(36, 37, 38), lake-cluster and landscape controls (39, 40), and broader abrupt-thaw settings (41). Temperature-conditioned precipitation–slump relations at Beiluhe further illustrate hydroclimatic nonlinearity (42). Compatibility is not attribution: inventories are incomplete, boundaries evolve, and mapping can contain false positives (43, 44, 45). Hydrothermal–deformation relations can also differ in nearby nonpermafrost (NPF) landslides (46). The unresolved lake × slump interaction argues against treating the 10 groups as causal process classes.

Not all extremes need be periglacial in origin. Within mapped NPF, the Tainan and Sebei gas-field anchors overlap part of the northern extreme population. Excluding their neighborhoods leaves the NPF threshold and recurrence direction intact and increases the fixed 3.25-km model-sample Zou transition/interior prevalence ratio. Thus, the tested mapped-NPF d_u threshold, boundary control, variable-group-ranking, and recurrence summaries do not depend on retaining those neighborhoods, but the analysis does not quantify any extraction contribution.

Environmental heterogeneity is domain- and context-dependent

Model responses cannot be summarized by one corridor-wide relation. Raw temperature variables carry the dominant NPF information, while local contrasts do not meet the prespecified incremental-skill criterion beyond it; in PF, adding contrasts yields modest but consistent held-out AP gains for both targets, notably in terrain, soil, wetness, and vegetation variable groups. Group-stratified summaries show where these relations differ: the d_u response to mean annual ground temperature concentrates near the mapped NPF transition, and the topographic wetness response changes direction between lake-only and several inventory-distal or dual-context PF groups. These model responses complement thermokarst susceptibility work (47) and interpretable deformation screening (48), while seasonal and active-layer studies address complementary targets or inversions (49, 50). They are held-out spatial associations, not evidence of physical causation.

Recurrence adds a population-level monitoring dimension

Among pixels retained after temporal quality control, approximately half of full-window extremes recur in both subwindows, and the point estimate of recurrence in the NPF transition exceeds that in the NPF interior under every support scheme. PF groups contain more window-specific signals without a stable ranking; sparse slump-related margin groups cannot support uncertainty estimates. The paired histories sharpen this contrast: across all supported mutually exclusive groups and overlapping aggregate populations, d_u-selected pixels accumulate separation from matched controls across all six annual intervals, whereas gradient-selected pixels show no systematic cross-geometry evolution in local differential line-of-sight displacement. The two tails therefore warrant different temporal interpretations. A 7-year tail can still reflect recurrent motion, a window-specific episode, changing observation support, model choice, or residual reconstruction error (51); the cross-tab remains descriptive because the same observations define the full and subwindow tails.

Implications for monitoring

The workflow is potentially transferable to other regional InSAR settings: define unusual motion relative to its mapped-domain background, retain raw-state or local-contrast predictors only where spatial holdouts support incremental discrimination, assign boundary and inventory contexts using explicit fallback rules, and distinguish recurrent from window-specific populations. Along QTEC, the concentration of 68–71% of NPF extremes near the mapped transition and transition recurrence of 59–62% among retained pixels support prioritizing this zone for repeated screening. Within PF, lake, slump, dual-inventory, and inventory-distal groups require separate interpretation: supported-group recurrence spans 31.5–41.9% for d_u and 38.3–47.3% for the gradient, and paired d_u-selected histories have annual-anchor trend magnitudes of ∼7–11 mm year^{-1} relative to matched controls. Groups with insufficient support indicate the need for additional observations rather than post hoc merging.

Limitations

No field survey, leveling record, GNSS measurement, or borehole series independently validates the tails; the 120–136-m products cannot resolve meter-scale discontinuities; and 2015–2021 may not represent longer-term behavior. North–south motion is unresolved under the two-component decomposition, spatial gradients amplify gaps and residual noise, maps and inventories are static and incomplete, and adjacent training and test blocks can meet at their edges. Breakpoint fallbacks, sparse ALE groups, and recurrence masks are reported explicitly; temporal inference is conditional on 42.6% of unmasked d_u and 40.2% of gradient support, and the paired histories compare extreme and matched-control pixels selected from the same 2015–2021 record used for evaluation. Sebei anchors lack contemporaneous production or pressure data, and all permutation, ALE, distance, interaction, recurrence, and paired-history results are observational. These limits preclude pixel-level attribution to thaw, thermokarst, slope motion, infrastructure, hydrology, extraction, or any single process.

Deramping does not establish a common reference between frames. Constant offsets cancel in within-frame line-of-sight gradients, but changes in frame contribution and viewing geometry can introduce artificial gradients at joins. Conditional reference and processing tests retain the broad geographic associations and consistent PF model improvement, while some rate-response directions and the NPF transition–interior recurrence difference are sensitive or unresolved. These tests do not establish absolute uncertainty or a common reference for the original rate product (SI Methods S1 and S9; Figs. S16 and S17; Tables S17–S20).

Within these constraints, the observed spatial organization and within-record recurrence can guide prioritization of follow-up observations, but not assignment of process, hazard, or infrastructure risk to individual pixels.

Downloaded from academic.oup.com/pnasnexus/article/5/11/pgag366/8997935 by Health Science Library of Peking University user on 10 November 2026

Materials and methods

InSAR deformation products and spatial context

The temporal archive contains 72 Sentinel-1 frames processed with ISCE2 and MintPy; temporal rates were refitted over 2015–2021 (52, 53, 54, 55) (SI Methods S1). The spatial rate product during 2015–2021 instead uses 12 ascending and seven descending line-of-sight rasters; their fitting/export linkage to the temporal archive remains unverified. We combined these rates in a two-component east/up decomposition that assumes zero north–south motion (56). We analyze the estimated up component, d_u, for which negative values denote downward motion. Because north–south motion remains unresolved, d_u should not be interpreted as a unique 3D vertical solution. Spatial-gradient magnitude was calculated by finite differences on the recovered native 135.648-m d_u grid without prior smoothing, before mapping to 136 m. This corrects the previous differentiation after coordinate snapping. Reference and processing sensitivities are reported in SI Methods S1 and S9, Figs. S16 and S17, and Tables S17–S20. A related preprint reports broader 2014–2022 processing and seasonal and active-layer analyses (14); the present study uses the authors' archived rate products and does not use that preprint's seasonal-amplitude or active-layer-thickness outputs. Contextual layers include the railway, two PF/NPF products, separate lake and slump inventories, and environmental variables (Figs. 1, S1, and S2; Table S1; SI Methods S2). VWC35 is modeled volumetric ground-ice content averaged over 3–5 m (36). It is excluded because uncertainty in amount and depth limits its representation of ice involved in local thaw. Its inclusion preserves the PF benefit from local contrasts; this does not imply that ground ice is physically unimportant (SI Methods S2 and S6; Table S16).

Domain separation and extreme definitions

The primary model sample, stratified by the Zou map, contains 90,000 mapped PF and 90,000 mapped NPF pixels with $d_u < 0$. Extremes are the within-domain 5% lower tail of d_u and 5% upper tail of the gradient (Fig. 2; Table S3); 1 and 10% tails bracket this choice. These labels identify distribution tails rather than events or mechanisms. Displayed values are rounded, while calculations use unrounded values. Finite native-grid gradients are available for 82,400 PF and 83,944 NPF pixels; missing gradients are excluded. Tail sensitivities are in Fig. S7, Table S9, and SI Methods S3.

Distance profiles and the 10-group partition

The distance analysis uses a fixed pixel-center sample every seventh 136-m source pixel (~0.952-km spacing) from the valid deformation footprint, including both upward and downward rates. Each sampled pixel represents equal area. The primary analysis applies the model-sample tail thresholds; thresholds recomputed on the systematic grid provide a sensitivity test. Signed boundary distance is retained for plotting; mapped class and unsigned distance assign groups. Lake and slump distances are measured to polygon area—lake-water pixels are excluded and slump interiors are assigned distance zero—with true polygon-edge distances used in sensitivity analyses.

For each target, constant, linear, and binomial hinge models with one change in slope are compared by the Bayesian information criterion (BIC) in 0.5-km bins; a breakpoint is retained only when it meets the prespecified ΔBIC, interval-width, count, block, and fold-direction criteria (equations and criteria in SI Methods S4). Lake or slump fits that do not meet these criteria use the predefined 2-km radius; PF-side boundary fits that do not meet them use the predefined target-specific operational widths of 3.25 km for d_u and 1.75 km for the gradient. Target-specific partitions and a fixed d_u partition assign NPF transition/interior and eight PF margin/interior × lake/slump contexts. Each eligible covered pixel receives exactly one label; uncovered or excluded pixels remain unassigned. Group area, prevalence, extreme share, object counts, membership sensitivity, and a block-bootstrap lake × slump interaction are reported in Figs. 3, S8, and S10, Tables S7, S10, and S12, and SI Methods S5.

The Cao map, Zou coordinate shifts from −3 to +3 km, and exclusion of 5-km buffers around Sebei anchors placed independently of the deformation field provide complementary sensitivity analyses. The Sebei test asks whether the mapped-NPF d_u threshold, fixed boundary control, variable-group-ranking, and recurrence summaries depend on the three gas-field-aligned neighborhoods, not how much extraction contributes (Fig. S15; Table S14). The earlier model-sample boundary comparisons use separate cutoffs (Fig. S4; Table S6; SI Methods S8).

Raw-state and local-contrast models

We fitted ExtraTrees classifiers (400 trees; balanced-subsample class weights; minimum leaf size 2) separately by domain and target (57). Missing values are replaced by each variable's median among training pixels. The 14 raw variables and 18 local contrasts form five groups: temperature, precipitation and wetness, vegetation and productivity, soil properties, and terrain and radiation (Table S2). Nine variables each supply a local SD and a gradient: ground temperature, wetness index, vegetation index, four soil properties, elevation, and slope. They were selected before model fitting to represent these environmental conditions. SD uses centered 5 × 5 neighborhoods (680 m); gradients are finite differences of neighborhood means, using source support up to 952 m, rather than fitted planes. SI Methods S6 specifies units and gap treatment. Boundary and inventory distances were excluded.

For the model comparison, raw-only, contrast-only, and combined models use identical training and held-out blocks under 12 schemes: 50-, 100-, and 150-km blocks, two grid origins, and two random seeds spanning data splitting, model fitting, and permutation. We report held-out AP, area under the receiver-operating-characteristic curve (AUROC), top-decile lift, Brier score, and 10-bin calibration error. Incremental contrast skill is classified as consistent when combined-minus-raw AP is positive in at least 9/12 schemes with a median gain >0.005; symmetric rules define degradation, negligible, or mixed results. Raw and contrast members

Downloaded from academic.oup.com/pnasnexus/article/5/11/pgag366/8997935 by Health Science Library of Peking University user on 10 November 2026

of each variable group are also permuted separately on held-out rows. Component importance is complementary because correlated predictors can exchange information (Figs. 4 and S9; Table S11). Each scheme withholds whole geographic blocks; schemes reuse pixels and are not independent replicates (SI Methods S6). Archived model-score maps are distinguished from updated diagnostics in Fig. S3 and Table S4.

Group-stratified ALE

Group-stratified models use the combined variables only where the preceding comparison supports incremental contrast skill; otherwise they use raw variables. Variables were specified before fitting: MAGT for NPF and the TWI and NDVI for PF. Total-domain and supported-group models use the same 12 schemes. A population requires at least 500 pixels, 30 extremes, and eight 50-km blocks; each split must also contain at least ten extremes in both training and testing. Populations that do not meet these requirements are reported as having insufficient support.

First-order ALE is evaluated on held-out rows (58). Effect strength is the root mean square of centered ALE values, with each input bin weighted by its share of evaluated pixels; direction is ALE(Q_{90})—ALE(Q_{10}). We retain the raw probability scale and normalize strength by the standard deviation of scores for evaluated pixels. A response is considered stable only when at least 9/12 schemes share a direction, with held-out AUROC $\geq$0.55 and AP lift $\geq$1.1. These are held-out model-response diagnostics, not causal effects (Figs. 4 and S6; Table S8; SI Methods S6).

Within-record temporal recurrence

Full (2015–2021), early (2015–2018), and late (2019–2021) rates were fitted from the same acquisitions in 72 image frames; geometry pairs meeting the predefined pixel-count, correlation, error, and slope criteria were decomposed to east/up, with each overlap pixel assigned the median of its available pair estimates (SI Methods S7). The primary support excludes a 2-km buffer around pair-count transitions and the top 5% of multipair disagreement. Recurrence is the fraction of full-window domain-specific extremes that are also extreme in both subwindows. Recurrence is evaluated across five support schemes; a paired equivalence test compares the primary 2-km and 1-km masks.

For the cross-tab, the fixed full-window d_u group raster is applied unchanged across all support schemes and both targets. Domain-specific 5% tail thresholds are estimated separately for each window on common support, and full-window extremes are classed as recurrent, early-only, late-only, or neither. Overall intervals use 500 complete-block resamples; group intervals use 1,999 complete 50-km-block resamples and are displayed only with at least 30 extremes and 8 extreme-containing blocks. The exact crosswalk between Fig. 2 pixels and temporal support is reported in Table S13 and SI Methods S7a.

From the fixed census of 388,637 extreme pixels, we deterministically sampled up to eight extremes per target, group, and 50-km block. The sample contains 4,940 unique pixels representing 4,968 selections across the two targets; each selection was paired with a nonextreme control from the same group, block, and radar-frame pair, within specified tolerances for terrain, railway distance, and observation counts. Native frame-level line-of-sight histories were extracted from the checksummed archive; fused products served only as quality assurance. The primary trend is the median pairwise slope among modeled displacement estimates on 25 May each year of the extreme-minus-control contrast, with equal radar-frame-pair weight within blocks, equal block weight within groups, 1,999 complete 50-km-block-bootstrap replicates, and predefined support and balance criteria. The gradient-selected response is the local differential line-of-sight history, not a planar-gradient time series; east/up anchors under the zero-north-motion approximation remain SI-only (SI Methods S7b; Figs. S12–S14; Table S15).

Acknowledgments

The authors thank Dr. Sayyed Mohammad Javad Mirzadeh for helping with early InSAR data preprocessing.

Supplementary Material

Supplementary material is available at *PNAS Nexus* online.

Competing Interest

The authors declare no competing interests.

Funding

This research is supported by the National Natural Science Foundation of China, grant 42371078, the Emerging Engineering Interdisciplinary Youth Program, Peking University, and the Program of the State Key Laboratory of Cryospheric Science and Frozen Soil Engineering, Chinese Academy of Sciences (CSFSE-KF-2414).

Author Contributions

Mei Chen (Conceptualization, Formal analysis, Investigation, Methodology, Software, Validation, Visualization, Writing—original draft, Writing—review & editing), and Xie Hu (Conceptualization, Data curation, Funding acquisition, Investigation, Supervision, Writing—review & editing)

Data Availability

The archived spatial rate raster and associated processing code are available at https://doi.org/10.5281/zenodo.21622603 (version 1.0.0). Further analyses of gradient calculation and multiframe sensitivity are documented in SI Methods S1 and S9, Figs. S16 and S17, and Tables S17 and S20. Original satellite, environmental, and geographic datasets are identified in Table S1. Licensed imagery sources, acquisition dates, and reuse exclusions are documented in the figure captions and SI Methods S2.

AI-assisted drafting disclosure

The authors used OpenAI ChatGPT/Codex and Anthropic Claude for language editing, code drafting and review, figure planning, and consistency checks. The authors reviewed all assisted

Downloaded from academic.oup.com/pnasnexus/article/5/11/pgag366/8997935 by Health Science Library of Peking University user on 10 November 2026

material, verified results against documented sources, determined the interpretation, and take responsibility for the manuscript.

References

1. Smith SL, O'Neill HB, Isaksen K, Noetzli J, Romanovsky VE. 2022. The changing thermal state of permafrost. *Nat Rev Earth Environ*. 3:10–23.
2. Biskaborn BK, *et al.* 2019. Permafrost is warming at a global scale. *Nat Commun*. 10:264.
3. Hjort J, *et al.* 2022. Impacts of permafrost degradation on infrastructure. *Nat Rev Earth Environ*. 3:24–38.
4. Hjort J, *et al.* 2018. Degrading permafrost puts Arctic infrastructure at risk by mid-century. *Nat Commun*. 9:5147.
5. Cheng G, Wu T. 2007. Responses of permafrost to climate change and their environmental significance, Qinghai-Tibet plateau. *J Geophys Res Earth Surf*. 112:F02S03.
6. Fu Z, *et al.* 2025. Non-temperature environmental drivers modulate warming-induced 21st-century permafrost degradation on the Tibetan Plateau. *Nat Commun*. 16:7556.
7. Jin H, Yu QH, Wang SL, Lü LZ. 2008. Changes in permafrost environments along the Qinghai-Tibet engineering corridor induced by anthropogenic activities and climate warming. *Cold Reg Sci Technol*. 53:317–333.
8. Jiang G, *et al.* 2024. Long-term responses of permafrost to the dual impacts of climate warming and engineering disturbance along the Qinghai-Tibet Highway. *Cold Reg Sci Technol*. 220:104135.
9. Wu Q, Zhang T, Liu Y. 2012. Thermal state of the active layer and permafrost along the Qinghai-Xizang (Tibet) Railway from 2006 to 2010. *Cryosphere*. 6:607–612.
10. Mu Y, *et al.* 2012. Thermal regime of conventional embankments along the Qinghai-Tibet railway in permafrost regions. *Cold Reg Sci Technol*. 70:123–131.
11. Wei Z, *et al.* 2021. Sentinel-based inventory of thermokarst lakes and ponds across permafrost landscapes on the Qinghai-Tibet Plateau. *Earth Space Sci*. 8:e2021EA001950.
12. Xia Z, *et al.* 2022. Retrogressive thaw slumps along the Qinghai-Tibet Engineering Corridor: a comprehensive inventory and their distribution characteristics. *Earth Syst Sci Data*. 14:3875–3887.
13. Zhang Z, Wang M, Wu Z, Liu X. 2019. Permafrost deformation monitoring along the Qinghai-Tibet Plateau Engineering Corridor using InSAR observations with multi-sensor SAR datasets from 1997–2018. *Sensors*. 19:5306.
14. Hu X, *et al.* 2025. Linking permafrost deformation to active layer freeze-thaw dynamics in the Qinghai-Tibet Engineering Corridor. egusphere-2025-4184. https://doi.org/10.5194/egusphere-2025-4184
15. Zwieback S, Liu L, Rouyet L, Short N, Strozzi T. 2024. Advances in InSAR analysis of permafrost terrain. *Permafr Periglac Process*. 35:544–556.
16. Liu S, *et al.* 2025. Ground surface deformation in permafrost region on the Qinghai-Tibet Plateau: a review. *Earth Sci Rev*. 265:105109.
17. Sadeghi Chorsi T, Meyer FJ, Dixon TH. 2024. Toward long-term monitoring of regional permafrost thaw with satellite interferometric synthetic aperture radar. *Cryosphere*. 18:3723–3740.
18. He P, Niu F, Huang Y, Zhang S, Jiao C. 2023. Distress characteristics in embankment-bridge transition section of the Qinghai-Tibet Railway in permafrost regions. *Int J Disaster Risk Sci*. 14:680–696.
19. Zou D, *et al.* 2017. A new map of permafrost distribution on the Tibetan Plateau. *Cryosphere*. 11:2527–2542.
20. Cao Z, Nan Z, Hu J, Chen Y, Zhang Y. 2023. A new 2010 permafrost distribution map over the Qinghai-Tibet Plateau based on subregion survey maps: a benchmark for regional permafrost modeling. *Earth Syst Sci Data*. 15:3905–3930.
21. Xia Z, *et al.* 2024. Widespread and rapid activities of retrogressive thaw slumps on the Qinghai-Tibet Plateau from 2016 to 2022. *Geophys Res Lett*. 51:e2024GL109616.
22. Zhou G, *et al.* 2024. Accelerating thermokarst lake changes on the Qinghai-Tibetan Plateau. *Sci Rep*. 14:2985.
23. Niu F, *et al.* 2014. Morphological characteristics of thermokarst lakes along the Qinghai-Tibet Engineering Corridor. *Arct Antarct Alp Res*. 46:963–974.
24. Li W, *et al.* 2025. Characteristic, relationship and impact of thermokarst lakes and retrogressive thaw slumps over the Qinghai-Tibetan Plateau. *Geoderma*. 457:117293.
25. Lu P, Han J. 2025. Remote sensing for identification and mapping of thermokarst landforms: a review. *Permafr Periglac Process*. 36:329–342.
26. Yin G, *et al.* 2021. Spatial analyses and susceptibility modeling of thermokarst lakes in permafrost landscapes along the Qinghai-Tibet Engineering Corridor. *Remote Sens (Basel)*. 13:1974.
27. Yin G, *et al.* 2023. High-resolution assessment of retrogressive thaw slump susceptibility in the Qinghai-Tibet Engineering Corridor. *Res Cold Arid Reg*. 15:288–294.
28. Jiang S, *et al.* 2024. How interpretable machine learning can benefit process understanding in the geosciences. *Earth's Future*. 12:e2024EF004540.
29. Roberts DR, *et al.* 2017. Cross-validation strategies for data with temporal, spatial, hierarchical, or phylogenetic structure. *Ecography*. 40:913–929.
30. Valavi R, Elith J, Lahoz-Monfort JJ, Guillera-Arroita G. 2019. blockCV: an R package for generating spatially or environmentally separated folds for k-fold cross-validation of species distribution models. *Methods Ecol Evol*. 10:225–232.
31. Stock A, Gregr EJ, Chan KMA. 2023. Data leakage jeopardizes ecological applications of machine learning. *Nat Ecol Evol*. 7:1743–1745.
32. Liu X, Hu J, Sun Q, Li Z, Zhu J. 2017. Deriving 3-D time-series ground deformations induced by underground fluid flows with InSAR: case study of Sebei gas fields, China. *Remote Sens (Basel)*. 9:1129.
33. Lin Z, Luo J, Niu F. 2016. Development of a thermokarst lake and its thermal effects on permafrost over nearly 10 yr in the Beiluhe Basin, Qinghai-Tibet Plateau. *Geosphere*. 12:632–643.
34. Ling F, Wu Q, Zhang T, Niu F. 2012. Modelling open-talik formation and permafrost lateral thaw under a thermokarst lake, Beiluhe Basin, Qinghai-Tibet Plateau. *Permafr Periglac Process*. 23:312–321.
35. Ke X, *et al.* 2025. Thermokarst lakes disturb the permafrost structure and stimulate through-talik formation in the

Downloaded from academic.oup.com/pnasnexus/article/5/11/pgag366/8997935 by Health Science Library of Peking University user on 10 November 2026

Qinghai-Tibet Plateau, China: a hydrogeophysical investigation. *Cryosphere*. 19:4989–5002.
36. Zou D, *et al.* 2024. Estimation of permafrost ground ice to 10 m depth on the Qinghai-Tibet Plateau. *Permafr Periglac Process*. 35:423–434.
37. Gao Z, Niu F, Wang Y, Lin Z, Wang W. 2021. Suprapermafrost groundwater flow and exchange around a thermokarst lake on the Qinghai-Tibet Plateau, China. *J Hydrol (Amst)*. 593: 125882.
38. Gao Z, Niu F, Wang Y, Luo J, Lin Z. 2017. Impact of a thermokarst lake on the soil hydrological properties in permafrost regions of the Qinghai-Tibet Plateau, China. *Sci Total Environ*. 574:751–759.
39. Ke X, Wang W, Huang W, Niu F, Gao Z. 2023. Thermokarst lakes group accelerates permafrost degradation in the Qinghai-Tibet Plateau, China: a modeling study. *J Hydrol (Amst)*. 625:130072.
40. Kokelj SV, Jorgenson MT. 2013. Advances in thermokarst research. *Permafr Periglac Process*. 24:108–119.
41. Turetsky MR, *et al.* 2020. Carbon release through abrupt permafrost thaw. *Nat Geosci*. 13:138–143.
42. Zhou Y, *et al.* 2026. Decoupling hydroclimatic controls on displacement of retrogressive thaw slumps in Qinghai-Tibet Plateau. *Geophys Res Lett*. 53:e2025GL119081.
43. Huang L, Luo J, Lin Z, Niu F, Liu L. 2020. Using deep learning to map retrogressive thaw slumps in the Beiluhe region (Tibetan Plateau) from CubeSat images. *Remote Sens Environ*. 237:111534.
44. Nitze I, *et al.* 2025. A labeling intercomparison of retrogressive thaw slumps by a diverse group of domain experts. *Permafr Periglac Process*. 36:83–92.
45. Lin Y, *et al.* 2025. Multi-annual inventorying of retrogressive thaw slumps using domain adaptation. *J Geophys Res Mach Learn Comput*. 2:e2024JH000370.
46. Ye X, *et al.* 2024. Near-surface soil hydrothermal response feedbacks landslide activity and mechanism. *Eng Geol*. 341: 107690.
47. Yang Y, *et al.* 2024. Susceptibility modeling and potential risk analysis of thermokarst hazard in Qinghai-Tibet Plateau permafrost landscapes using a new interpretable ensemble learning method. *Atmosphere (Basel)*. 15:788.
48. Lin X, *et al.* 2025. Revealing the impacts of environmental and anthropogenic factors on permafrost deformation in the central Qinghai-Tibet Plateau using InSAR and interpretable machine learning. *Ecol Indic*. 178:113977.
49. Chang T, *et al.* 2024. Unraveling the non-linear relationship between seasonal deformation and permafrost active layer thickness. *NPJ Clim Atmos Sci*. 7:308.
50. Peng S, *et al.* 2023. Using InSAR for surface deformation monitoring and active layer thickness retrieval in the Heihe River Basin on the Northeast Qinghai-Tibet Plateau. *J Geophys Res Earth Surf*. 128:e2022JF006782.
51. Fan C, *et al.* 2025. Time-series models for ground subsidence and heave over permafrost in InSAR processing: a comprehensive assessment and new improvement. *ISPRS J Photogramm Remote Sens*. 222:167–185.
52. Torres R, *et al.* 2012. GMES Sentinel-1 mission. *Remote Sens Environ*. 120:9–24.
53. Rosen PA, *et al.* The InSAR scientific computing environment. In: Proceedings of the 9th European Conference on Synthetic Aperture Radar (EUSAR 2012); Nuremberg, Germany. VDE; 2012. p. 730–733.
54. Yunjun Z, Fattahi H, Amelung F. 2019. Small baseline InSAR time series analysis: unwrapping error correction and noise reduction. *Comput Geosci*. 133:104331.
55. Berardino P, Fornaro G, Lanari R, Sansosti E. 2002. A new algorithm for surface deformation monitoring based on small baseline differential SAR interferograms. *IEEE Trans Geosci Remote Sens*. 40:2375–2383.
56. Wright TJ, Parsons BE, Lu Z. 2004. Toward mapping surface deformation in three dimensions using InSAR. *Geophys Res Lett*. 31:L01607.
57. Geurts P, Ernst D, Wehenkel L. 2006. Extremely randomized trees. *Mach Learn*. 63:3–42.
58. Apley DW, Zhu J. 2020. Visualizing the effects of predictor variables in black box supervised learning models. *J R Stat Soc Series B Stat Methodol*. 82:1059–1086.

Downloaded from academic.oup.com/pnasnexus/article/5/11/pgag366/8997935 by Health Science Library of Peking University user on 10 November 2026